nature energy

ARTICLES

https://doi.org/10.1038/s41560-019-0538-4

Managing grains and interfaces via ligand anchoring enables 22.3%-efficiency inverted perovskite solar cells

Xiaopeng Zheng[1,6], Yi Hou[2,6], Chunxiong Bao[3], Jun Yin[1], Fanglong Yuan[2,4], Ziru Huang[2], Kepeng Song[1], Jiakai Liu[1], Joel Troughton[1], Nicola Gasparini[1], Chun Zhou[2], Yuanbao Lin[1], Ding-Jiang Xue[2], Bin Chen[2], Andrew K. Johnston[2], Nini Wei[5], Mohamed Nejib Hedhili[5], Mingyang Wei[2], Abdullah Y. Alsalloum[1], Partha Maity[1], Bekir Turedi[1], Chen Yang[1], Derya Baran[1], Thomas D. Anthopoulos[1], Yu Han[1], Zheng-Hong Lu[4], Omar F. Mohammed[1], Feng Gao[3], Edward H. Sargent[2*] and Osman M. Bakr[1*]

Inverted perovskite solar cells have attracted increasing attention because they have achieved long operating lifetimes. However, they have exhibited significantly inferior power conversion efficiencies compared to regular perovskite solar cells. Here we reduce this efficiency gap using a trace amount of surface-anchoring alkylamine ligands (AALs) with different chain lengths as grain and interface modifiers. We show that long-chain AALs added to the precursor solution suppress nonradiative carrier recombination and improve the optoelectronic properties of mixed-cation mixed-halide perovskite films. The resulting AAL surface-modified films exhibit a prominent (100) orientation and lower trap-state density as well as enhanced carrier mobilities and diffusion lengths. These translate into a certified stabilized power conversion efficiency of 22.3% (23.0% power conversion efficiency for lab-measured champion devices). The devices operate for over 1,000 h at the maximum power point under simulated AM1.5 illumination, without loss of efficiency.

Metal halide perovskite semiconductors have seen rapid progress in their optoelectronic applications due to their broadly tunable compositions achieved using simple processing approaches[1,2], and in light of their strong light absorption[3], high charge mobility[4] and long carrier diffusion lengths[5–7]. In photovoltaics (PVs), the power conversion efficiency (PCE) of single-junction perovskite solar cells (PSCs) started at 3.8% in 2009 and has now reached 25.2% (refs. [1,8]).

The highest-efficiency devices use the regular (n–i–p) structure. However, removing ionically doped hole transport materials in inverted (p–i–n) devices has contributed to recent advances in device operating stability[9]. Recently, Bai et al. reported long-term operationally stable inverted PSCs with a PCE loss of less than 5% under continuous simulated AM1.5 irradiation for more than 1,800 h at 70–75 °C in the efficiency dervied from the current density–voltage (J–V) relationship[10]. Yang et al. reported inverted PSCs that maintained 97% of the initial efficiency after operation at the maximum power point (MPP) under simulated AM1.5 irradiation for 1,200 h at 65 °C (ref. [11]). Unfortunately, the PCEs of inverted PSCs lag significantly behind those of regularly structured devices (20.9% vs 25.2%, according to certified records)[8,12–14]. Photo-voltage loss due to non-radiative recombination of photogenerated charge carriers is a key factor in the inferior PCEs of inverted PSCs, despite various attempts at addressing this issue[13,15].

The photo-voltage of a solar cell depends on the splitting of the electron (E_{Fn}) and hole (E_{Fp}) quasi-Fermi levels of its photoactive layer. This splitting is a function of the steady-state charge density and the bandgap of the absorber. Nonradiative carrier recombination impairs charge-density buildup and diminishes the device's photo-voltage. Electronic trap states caused by crystallographic defects including point defects or higher-dimensional defects (such as grain boundaries) are sources of non-radiative charge-carrier recombination; numerous studies have pointed to the critical role of the passivation of point defects and grain boundaries in achieving high-efficiency PSCs[12,16–20]. These defect sites not only militate against a high photo-voltage, but also shorten the operational lifetime of perovskite devices, as they present a vulnerable initiation site for degradation by extrinsic environmental species[21–23].

Here we demonstrate the use of long AALs with an optimized alkyl-chain length as grain and interface modifiers to improve optoelectronic properties by promoting favourable grain orientation and suppressing trap-state density. These augmented film properties enable the demonstration of a record certified PCE of >22.3% (23.0% PCE for lab-measured champion devices) for inverted-structured devices. The devices show no PCE loss after 1,000 h of operation at the MPP under simulated AM1.5 illumination.

[1]Division of Physical Sciences and Engineering, King Abdullah University of Science and Technology (KAUST), Thuwal, Saudi Arabia. [2]Department of Electrical and Computer Engineering, University of Toronto, Toronto, Ontario, Canada. [3]Department of Physics, Chemistry and Biology (IFM), Linköping University, Linköping, Sweden. [4]Department of Materials Science and Engineering, University of Toronto, Toronto, Ontario, Canada. [5]Imaging and Characterization Core Lab, King Abdullah University of Science and Technology (KAUST), Thuwal, Saudi Arabia. [6]These authors contributed equally: Xiaopeng Zheng, Yi Hou. *e-mail: ted.sargent@utoronto.ca; osman.bakr@kaust.edu.sa

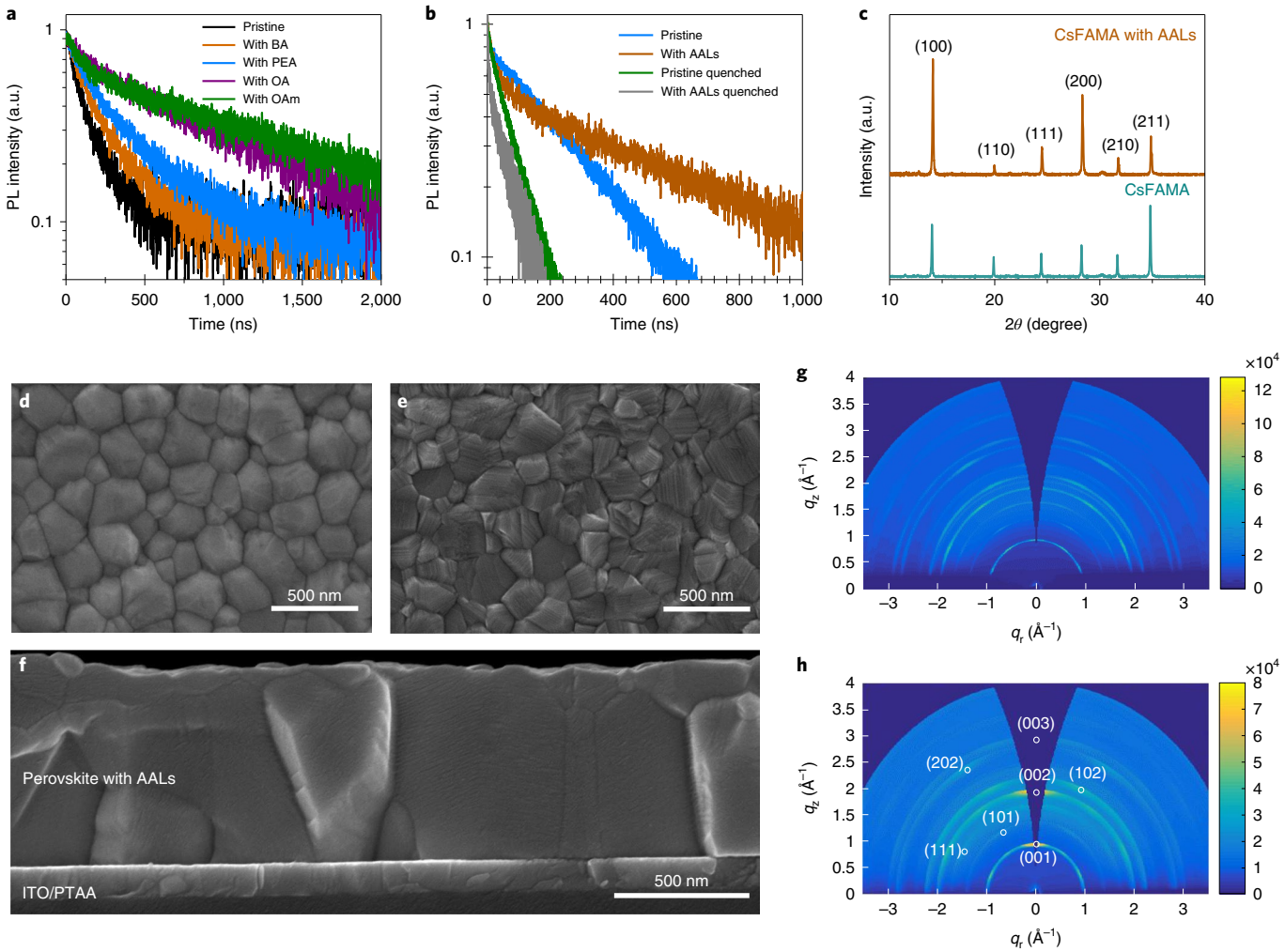

Fig. 1 | Optical and structural characterization of perovskite films with AALs. a, TRPL decay curves of CsFAMA films with AALs with different alkyl-chain lengths. **b**, TRPL decay curves for the pristine CsFAMA film, CsFAMA film with AALs, quenched pristine film and quenched film with AALs. A PCBM layer was spin coated on the perovskite film surface for the quenched films. **c**, XRD patterns of the pristine CsFAMA film and the CsFAMA film with AALs. **d**,**e**, Top-view SEM images of the pristine CsFAMA film (**d**) and the CsFAMA film with AALs (**e**). **f**, Cross-sectional SEM image of the CsFAMA film with AALs. **g**,**h**, GIWAXS maps of the pristine CsFAMA film (**g**) and the CsFAMA film with AALs (**h**). The indexed facets are marked with white circles and labelled. The colour scale bar represents the higher diffraction intensity.

Optical and structural properties of AAL-treated perovskites

AALs have a long alkyl hydrophobic chain as well as an amine group capable of anchoring to the A-site of perovskites. Molecules with an amine group have been implicated in promoting specific facets for perovskite films and single crystals[24,25], and also filling point defects (A-site vacancies can potentially be filled by amine groups)[26,27]. After the self-assembly of AALs in the perovskite matrix, the molecular modified perovskite interfaces are composed of densely packed ligands that are stabilized by van der Waals interactions between hydrophobic organic moieties of the ligands. Such van der Waals interactions become stronger with increasing alkyl-chain length[28]. This thin insulating layer (quantum tunnelling layer) on the surfaces and grain boundaries suppresses nonradiative charge-carrier recombination[19,28–31] and acts as an ion migration barrier[32,33]. The alkyl-chain length influences the ligand packing density, ligand desorption energy, carrier dynamics and ion migration, and eventually impacts the device efficiency and stability[28,33–38]. Therefore, as a proof-of-concept, we first studied the influence of AALs with different alkyl-chain lengths, namely *n*-butylamine (BA), phenethylamine (PEA), octylamine (OA) and oleylamine (OAm), on the perovskite film quality.

In contrast with procedures that are meant to generate a 2D/3D perovskite heterostructure, we only introduced a trace amount of AALs, <0.3 mol.%. Over 5 mol.% large A-site cations is typically required to form 2D/3D heterostructures[19,39–41]. $Cs_{0.05}(FA_{0.92}MA_{0.08})_{0.95}Pb(I_{0.92}Br_{0.08})_3$ (referred to as CsFAMA; FA, formamidinium; MA, methylammonium) was used as the baseline perovskite composition. The AALs (0.1 wt%) were directly added into the perovskite precursor, and the perovskite films were fabricated using a one-step anti-solvent crystallization approach[42].

We first used time-resolved photoluminescence (TRPL; Fig. 1a) to roughly assess the perovskite films' quality after introducing AALs with different alkyl-chain lengths. The perovskite films with long-alkyl-chain AALs (OA or OAm) exhibit carrier lifetimes (τ) that are much longer (OA, $\tau = 789$ ns; OAm, $\tau = 1{,}049$ ns) than those of pristine films ($\tau = 114$ ns) and of films with short-alkyl-chain AALs (BA, $\tau = 195$ ns; PEA, $\tau = 265$ ns). This indicates that the carrier nonradiative recombination was significantly suppressed upon the introduction of a trace amount of long-alkyl-chain AALs.

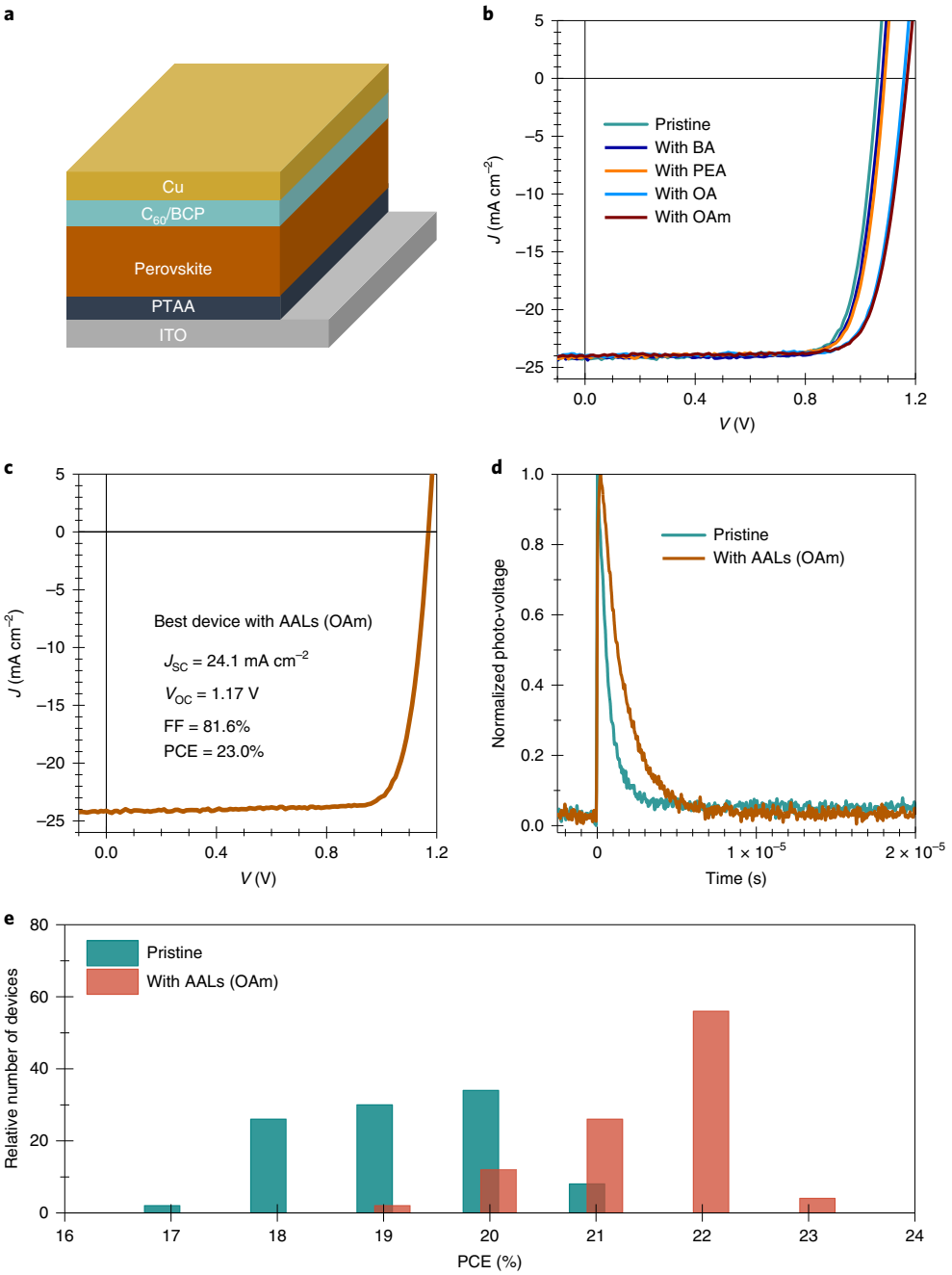

Fig. 2 | Device structure and PV performance analysis. a, The device architecture of inverted planar heterojunction PSCs. **b**, *J*–*V* characteristics of CsFAMA devices with the addition of AALs with different alkyl-chain lengths. **c**, *J*–*V* curves of the champion CsFAMA device with AALs. **d**, Transient photo-voltage measurement of CsFAMA devices without and with AALs. **e**, The statistics of PCE distribution for 100 devices (50 pristine devices and 50 devices with AALs).

Supplementary Fig. 1 shows the water contact angles of perovskite films with AALs of different alkyl-chain lengths (0.1 wt%). The water contact angle for the pristine film is 60°, and it increased to 63° and 71° for the perovskite films with BA and PEA, respectively, which are short-alkyl-chain AALs. By contrast, the perovskite films with long-alkyl-chain AALs exhibited much larger water contact angles: 88° and 98° for the perovskite films with OA and OAm, respectively. This observation indicates that the long-alkyl-chain AALs assembled on the perovskite film surface, thus dramatically enhancing the hydrophobicity of the films. The water contact angles (Supplementary Fig. 2) for the perovskite films with 0.05 wt% and 0.2 wt% AALs are 97° and 100°, respectively, suggesting a similar coverage of anchoring AAL molecules after anti-solvent washing.

The distinct improvement of film quality motivated us to investigate the unique role of the trace amount of long-alkyl-chain AALs. For the rest of the discussion, AAL refers to OAm unless otherwise noted. Figure 1d,e shows scanning electron microscopy (SEM) images of CsFAMA films without and with the introduction of AALs. The films with AALs show a similar grain size to that of pristine films. The SEM image cross-section (Fig. 1f) shows a 750-nm-thick, highly crystalline perovskite absorber layer with a single grain throughout the thickness of the film. The powder X-ray diffraction

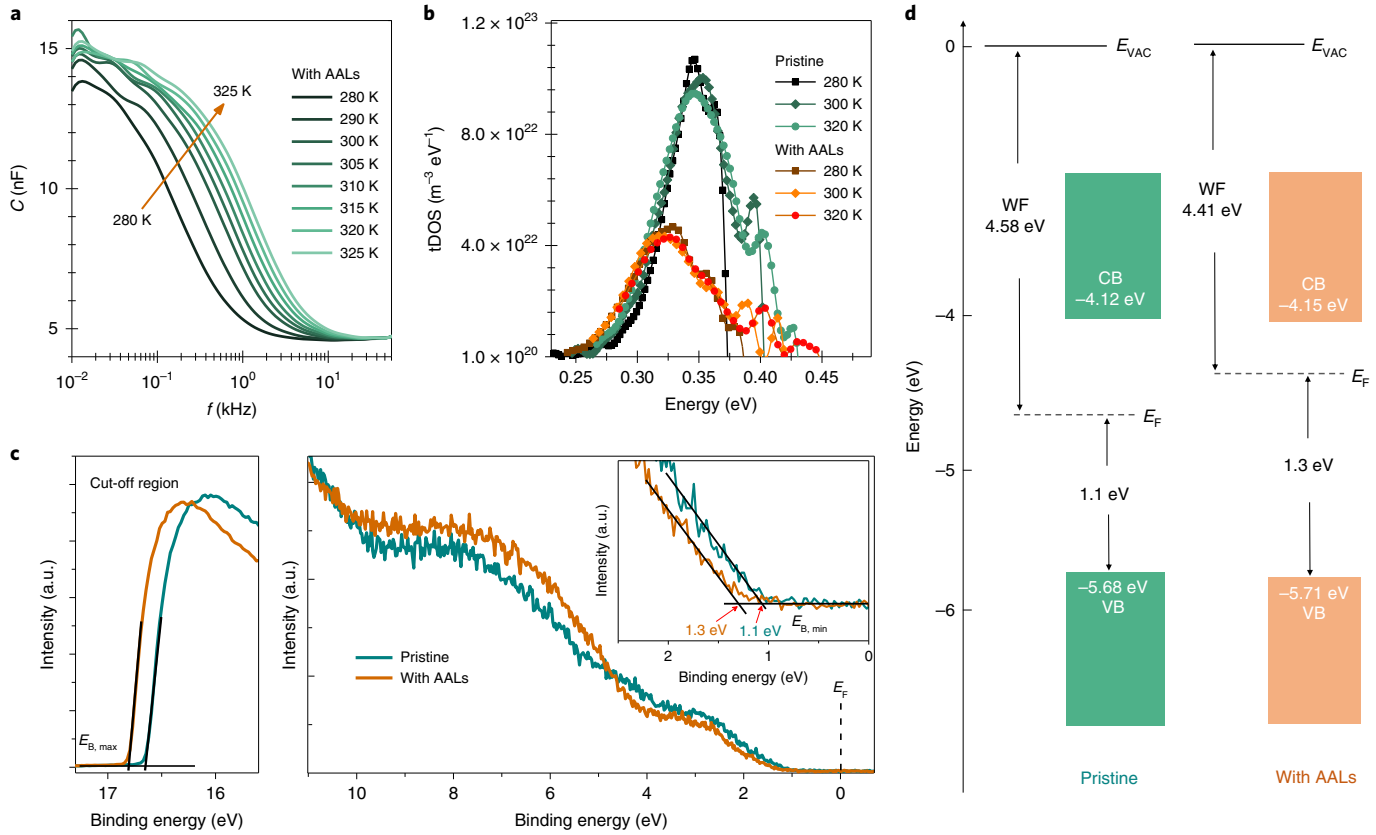

Fig. 3 | Defect density and energy-level characterization of perovskite films with AALs. a, Temperature-dependent *C*–*f* plots for a CsFAMA device with AALs. **b**, Trap density of states (tDOS) deduced from temperature-dependent *C*–*f* plots for the pristine CsFAMA device and the CsFAMA device with AALs. **c**, UPS data for the pristine CsFAMA film and the film with AALs. Helium Iα ($h\nu = 21.22$ eV) spectra of secondary electron cut-off (left panel) and UPS spectra in the valence band (VB) region (right panel) are shown. The inset shows the enlarged UPS spectra in the VB region, and the intercept indicates the distance of the VBM with respect to E_F, which was noted as $E_{B,min}$. The intercept in the secondary electron cut-off (left panel) shows $E_{B,max}$, and the WF was obtained by $h\nu - E_{B,max}$. The VBM was obtained by $h\nu - (E_{B,max} - E_{B,min})$. The position of the CBM with respect to the VBM was defined by the optical bandgap (1.56 eV). **d**, Energy-level scheme for the pristine CsFAMA film and the film with AALs based on the parameters derived from UPS spectra.

(XRD; Fig. 1c) patterns show a notably increased ratio of the (100) plane to the other crystal planes' peaks ((110), (111), (210) and (211)) in the films with AALs, which indicates that the (100) grains grew faster by consuming neighbouring, randomly oriented grains. Since powder XRD conveys information primarily from the film's bulk, we also used grazing-incidence wide-angle X-ray scattering (GIWAXS; Fig. 1g,h and Supplementary Fig. 3) to study the surface of the perovskite films. GIWAXS analysis of the films confirmed that the promotion of (100) occurred while other random orientations were suppressed; moreover, no signal that could be attributable to a 2D component was detected. In reported 2D/3D perovskites, 2D perovskite platelets can be observed in SEM images and a clearly detectable 2D component signal appears in GIWAXS[19,43]. However, we did not observe evidence of a 2D component formation from either SEM images or GIWAXS upon the introduction of trace amounts of AALs, which indicates that 2D perovskite is effectively absent from our films.

The absorption of the CsFAMA films is unaltered by the introduction of AALs (Supplementary Fig. 4). The Tauc plot from the ultraviolet–visible (UV–Vis) absorption spectra shows an optical bandgap of 1.56 eV for CsFAMA films. The steady photoluminescence (PL; Supplementary Fig. 5) intensity was significantly increased for films with AALs, indicating that the population of non-radiative recombination centres in the perovskite films was reduced. PL mapping confirmed the uniformly enhanced PL intensity as shown in Supplementary Fig. 6.

We hypothesized that a suppressed trap-state density and promoted (100) grain orientation resultant from the use of AALs may influence carrier transport in the perovskite films. We conducted contactless measurements of the photocarrier transport properties of CsMAFA-8 films, in which [6,6]-phenyl-C61-butyric acid methyl ester (PCBM) was used to induce the interfacial PL quenching[44,45], as shown in Fig. 1b. TRPL decay measurements show that the carrier lifetime without the quencher (τ) increased from 290 ns for the pristine films to 520 ns for the films with AALs. The quench-limited diffusion time (τ_q) was 80 and 50 ns for the pristine films and the films with AALs, respectively. From the equation[45] $L_D \approx \frac{2L}{\pi}\sqrt{2\left(\frac{\tau}{\tau_q} - 1\right)}$, where L_D and L stand for diffusion length and film thickness (~750 nm), respectively, we estimate a diffusion length of ~1 μm and ~2 μm for the pristine film and the film with AALs, respectively. Combining the relation $L_D = \sqrt{D \times \tau}$ and the Einstein relation $D = \mu \times k_B \times T/q$, where μ, k_B, T and q stand for mobility, Boltzmann's constant, temperature and elementary charge, respectively, we extracted a carrier mobility of 1.6 and 3 cm^2 V^{-1} s^{-1} for pristine films and films with AALs, respectively. Thus, CsMAFA-8 films containing AALs exhibited noticeably longer diffusion lengths and higher carrier mobilities than pristine films.

PV performance of AAL-treated perovskites

The improved carrier transport in AAL-treated films motivated us to investigate whether this enhancement in basic properties

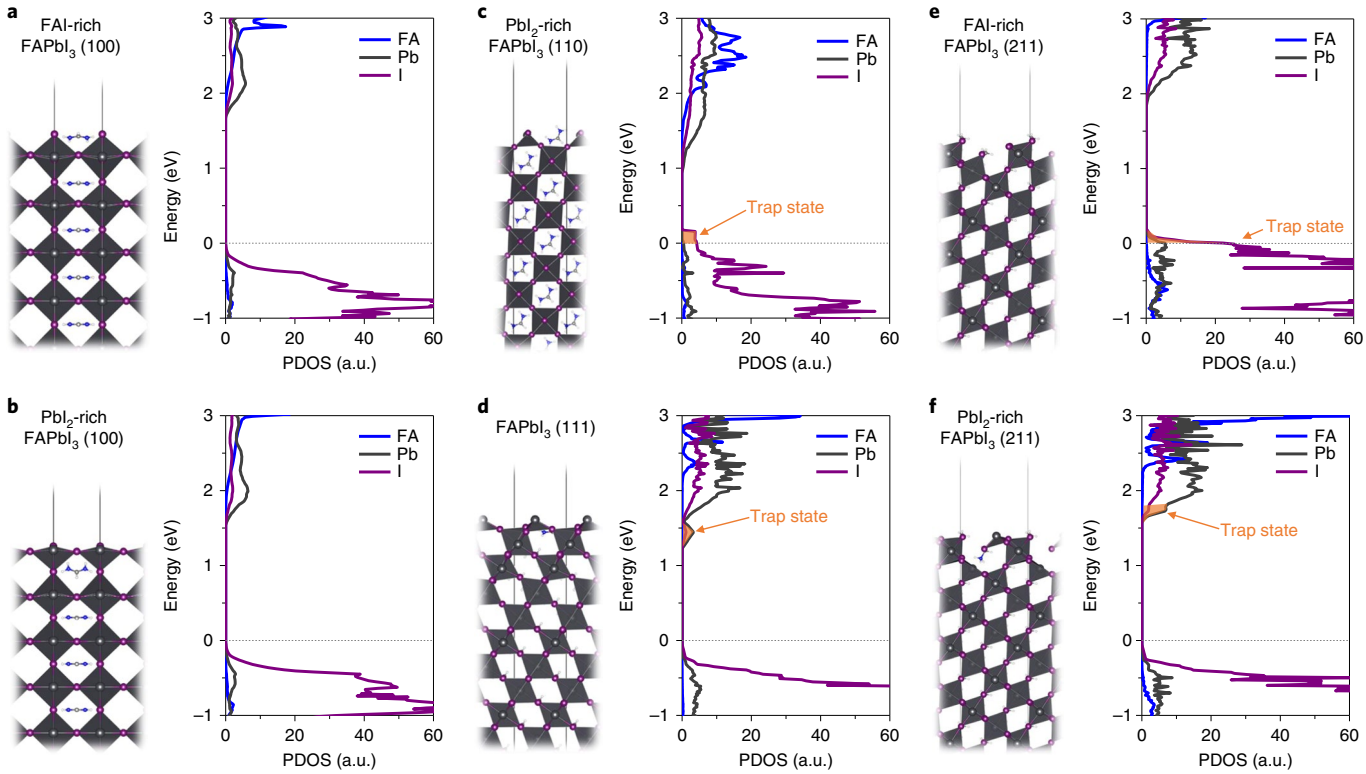

Fig. 4 | DFT calculation of the trap states on the surface of various crystallographic facets. a–f, Optimized crystal structures (left panel) and PDOS (right panel) with contributions from FA (blue), I (purple) and Pb (dark grey) of cubic-phase $FAPbI_3$ slabs with surface facets: FAI-rich (100) (**a**), PbI_2-rich (100) (**b**), PbI_2-rich (110) (**c**), $FAPbI_3$ (111) (**d**), FAI-rich (211) (**e**) and PbI_2-rich (211) (**f**) calculated by DFT. The trap states are marked with orange. The two straight grey lines in the crystal structure define the unit slab. The VBM is set at zero energy with a horizontal grey dashed line as a guide.

could be translated into improvements in device PCE, particularly through gains in photo-voltage. We fabricated PSCs based on CsFAMA films. As shown in Fig. 2a, the p–i–n planar heterojunction devices were structured as indium tin oxide (ITO) glass substrate/poly(triaryl amine) (PTAA)/perovskite/fullerene (C_{60})/bathocuproine (BCP)/copper.

Figure 2b shows the typical J–V characteristics of CsFAMA devices with AALs of different alkyl-chain lengths. The pristine devices show a typical PCE of 20.5% with a short-circuit current density (J_{SC}) of 24.2 mA cm^{-2}, an open-circuit voltage (V_{OC}) of 1.06 V and a fill factor (FF) of 80%. The performance of the CsFAMA devices with short-alkyl-chain AALs (BA or PEA) slightly improved to 20.8% (BA) and 20.9% (PEA), benefiting from ~30 mV V_{OC} enhancement. The PEA-concentration-dependent J–V characteristics of CsFAMA devices with PEA are shown in Supplementary Fig. 7. The champion device with PEA shows a V_{OC} and PCE of 1.15 V and 21.3%, respectively. By contrast, the devices with long-alkyl-chain AALs (OA or OAm) show a remarkably enhanced PCE, resulting from a strong V_{OC} improvement up to 110 mV. The devices with OAm show an average PCE around 22.0% with a J_{SC} of 24.1 mA cm^{-2}, a V_{OC} of 1.17 V and an FF of 78.2%. The champion devices with OAm deliver a PCE of 23% with a J_{SC} of 24.1 mA cm^{-2}, a V_{OC} of 1.17 V and an FF of 81.6%, as shown in Fig. 2c. The statistical PCE values from 100 devices (50 pristine devices and 50 devices with AALs; Fig. 2e) demonstrate the reproducibility of the performance enhancement associated with the use of AALs. The PCEs of the devices with OA are similar to those of the devices containing OAm, confirming the advantage of using long-alkyl-chain AALs over AALs with short chains. This is also in accordance with the trend of film quality as deduced from TRPL.

The voltage deficit is defined by $(E_g/q) - V_{OC}$, where E_g is the optical bandgap. Since the optical bandgap is 1.56 eV, the voltage deficit is only 0.39 V for devices based on long-alkyl-chain AALs.

When fine-tuning the concentration of long-alkyl-chain AALs from 0.05 wt% to 0.2 wt%, we did not observe an appreciable variation in device performance (Supplementary Fig. 8). Further increasing the AAL concentration to 0.4 wt% leads to a severe PCE drop.

Unencapsulated CsFAMA devices with AALs were certified at an accredited laboratory (Newport Photovoltaic Testing and Calibration Laboratory). The PCE certification protocol uses a quasi-steady-state (QSS) I–V sweep, instead of the normally used forward and reverse I–V scans, to ascertain a device's PV characteristics. Ten voltage points were collected in the QSS measurement, with each bias voltage applied and held until the measured current stabilized (Supplementary Fig. 9). The devices show a certified stabilized PCE of 22.34% with a J_{SC} of 23.9 mA cm^{-2}, a V_{OC} of 1.14 V and an FF of 82%, representing a record PCE for p–i–n-structured devices. The certified QSS I–V curve and external quantum efficiency (EQE) spectra are shown in Supplementary Fig. 10.

To identify the major factors responsible for the efficiency enhancement, we started by comparing the morphology (by top-view and cross-sectional SEM images) of the pristine perovskite films and the films with AALs (Supplementary Fig. 11). Both the pristine perovskite films and the films with AALs are compact with similar grain sizes. The full width at half maximum values of the (100) XRD peaks of pristine films and of films with AALs are 0.09° and 0.10°, respectively; that is, they are nearly identical. We can therefore rule out a major influence of perovskite grain size and crystallinity in this study.

To investigate the influence of surface passivation while avoiding effects related to perovskite film orientation, we subjected ready-formed pristine perovskite films to a post-treatment using AALs

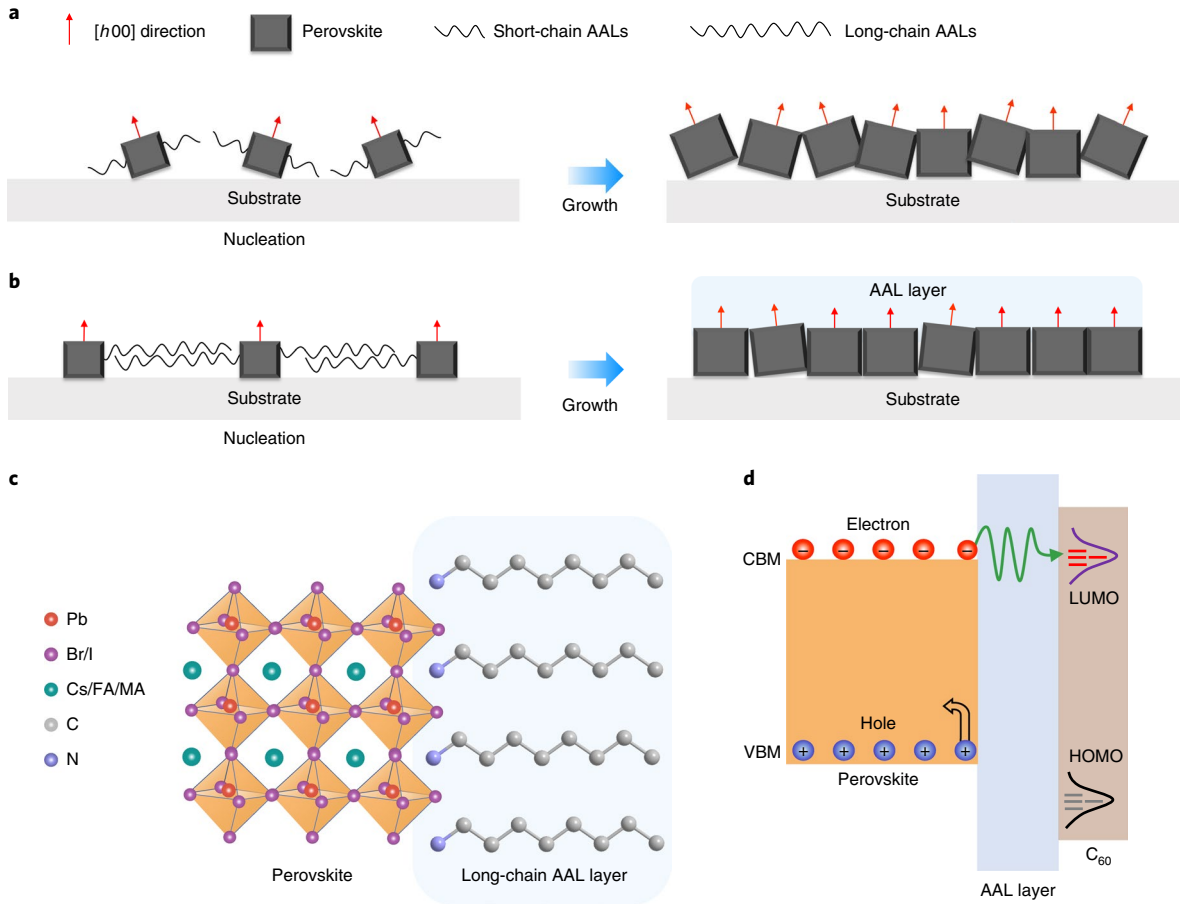

Fig. 5 | Schematic illustration of the likely mechanisms underpinning efficiency enhancements. a,**b**, Illustration of the influence of the short-chain AALs (**a**) and long-chain AALs (**b**) on the crystallization of the perovskite films. **c**,**d**, Illustration of long-chain AALs assembled on perovskite film surface (**c**) and blocking the holes at the perovskite and C_{60} interfaces (**d**). HOMO and LUMO stand for highest occupied molecular orbital and lowest unoccupied molecular orbital, respectively.

with alkyl chains of various lengths (BA, PEA and OAm). XRD patterns (Supplementary Fig. 12a) show that the films post-treated with AALs of different lengths had similar orientations to the pristine films. We then fabricated the devices based on these films with similar orientations.

The devices with post-treatment surface passivation enabled by AALs show higher PCE values than the pristine devices, and the long-chain AALs show better passivation, something we assign to stronger hole blocking at the interfaces between perovskite and C_{60} (Supplementary Fig. 12b)[31]. The V_{OC} and PCE of the devices with long-chain AALs increased to 1.12 V and 21.1%, respectively, post-treatment. However, in contrast with the devices fabricated by adding AALs into the precursor (V_{OC} of 1.17 V and PCE of >22%), the V_{OC} and PCE of devices with AAL surface passivation are still lower, indicating that surface passivation alone does not fully explain the performance improvement, and that tuning the orientation of the perovskite films plays a crucial role.

We conclude that the combined effect of both surface passivation and orientation tuning leads to the dramatically improved V_{OC} and PCE for the devices with AALs (mixed in the precursor). This result is rationalized by the facet dependence of the surface-defect density, and it highlights the crucial role of controlling the film orientation.

Mechanisms underpinning efficiency enhancements

We sought to evaluate whether changes in surface roughness had a significant role in improving the device efficiency. Atomic force microscopy images revealed that the roughness of films was reduced from 17.5 nm to 12.1 nm by introducing AALs (Supplementary Fig. 13), which suggests that changes in the interfacial roughness were not a major variable affecting the device performance.

To further elucidate the trap-state distributions and energies that are affected by the AAL treatment, we investigated trap-state profiles using thermal admittance spectroscopy. We acquired temperature-dependent capacitance versus frequency (C–f) plots to probe trap density and the energy depth of trap states (Fig. 3a and Supplementary Fig. 14). Figure 3b shows trap density profiles at different temperatures, deduced from the temperature-dependent C–f plots. At all temperatures from 280 to 320 K, the devices with AALs show a similar trap-state density at energies between 0.25 and 0.32 eV and a lower trap-state density across the higher-energy region from 0.32 to 0.4 eV. At room temperature (300 K), pristine devices show a peak trap density of $1 \times 10^{23}\,m^{-3}\,eV^{-1}$ at 0.35 eV; by contrast, the devices with AALs show a smaller peak intensity of $4.4 \times 10^{22}\,m^{-3}\,eV^{-1}$ at shallower energy (0.32 eV). The pristine devices show a trap-state density that is as much as approximately four times higher in the deeper energy region from 0.32–0.4 eV.

We further measured the electroluminescence (EL) spectra of solar cells operating as light-emitting diodes (LEDs), as shown in Supplementary Fig. 15. The devices with AALs deliver an EQE_{EL} of 0.65% under an injection current around J_{SC}. In comparison, the pristine devices show an EQE_{EL} of 0.07% under the same injection current. The V_{OC} improvement, ΔV_{OC}, estimated by $\Delta V_{OC} = (k_B T/q) \times \ln(EQE_{AALs}/EQE_{pristine})$ is ~60 mV.

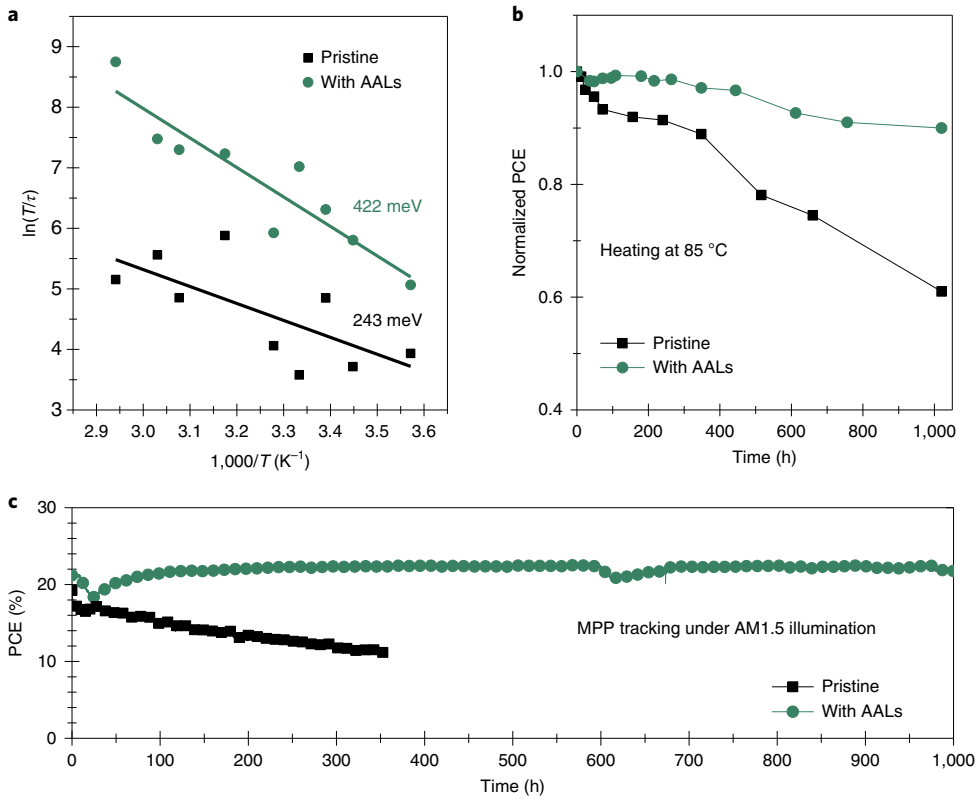

Fig. 6 | Ion migration and long-term device stability. a, Arrhenius plots (obtained by linear fitting of data points) of the temperature dependence of T/τ, showing an ion migration activation energy (E_a) of 243 meV and 422 meV for pristine films and films with AALs, respectively. Note that $1/\tau$ is the decay rate (s^{-1}). **b**, Thermal stability of devices at a fixed temperature of 85 °C in a nitrogen atmosphere. The data points (colour-filled dots) were collected by measuring the *J*–*V* curves of the samples at different time intervals. The initial PCEs are about 17% for the pristine CsFAMA device and 18% for the CsFAMA device with AALs. **c**, Plot showing 1,000 h of continuous MPP tracking for the pristine CsFAMA device and the CsFAMA device with AALs under constant simulated solar illumination (100 mW cm^{-2}) in a nitrogen atmosphere with a UV filter with a 420-nm cut-off. The initial PCEs are about 19.2% for the pristine CsFAMA device and 21.2% for the CsFAMA device with AALs.

To further test the carrier lifetime in fully operating devices, transient photo-voltage decay measurements were conducted. As seen in Fig. 2d, the carrier lifetime (τ) increased from 0.67 µs to 1.5 µs after introducing AALs. Light-intensity-dependent V_{OC} was measured and the diode ideal factor (n) was derived, as shown in Supplementary Fig. 16. When purely radiative recombination is present, n equals 1. The devices with AALs show n closer to 1 compared with the pristine devices, arising from the suppressed nonradiative recombination achieved by AALs.

AALs have the potential to suppress trap density directly by filling in A-site vacancies and modifying grains and interfaces. Additionally, they have the potential to provide a similar benefit by promoting the (100) orientation of grains in perovskite films[46], which may have a different susceptibility to surface-defect formation than other random orientations in the pristine perovskite films[47,48]. To further investigate this possibility, we studied the dependence of trap density on the surface crystallographic facets using density functional theory (DFT) calculations based on a cubic $FAPbI_3$ model[49,50]. The corresponding slabs exposing the (100), (110), (111), (210) and (211) surfaces were considered. From the projected density of states (PDOS) of all the slabs, as shown in Fig. 4 and Supplementary Figs. 17 and 18, we find that the valence band maximum (VBM) and the conduction band minimum (CBM) are mainly composed of I-5*p*, Pb-6*s* and Pb-6*p* orbitals. According to these modelling results, some surfaces are less benign than others; the (110) (Fig. 4c), (111) (Fig. 4d) and (211) (Fig. 4e,f) surfaces show trap states that are more likely to adversely affect device performance. However, there are no trap states that appear for the (100) surface in either FAI-rich or PbI_2-rich termination cases (Fig. 4a,b). Thus, it can be concluded that the (110), (111) and (211) surfaces would introduce additional trap states, while in the case of the (100) surface, the delocalized electronic distributions of the VBM and the CBM are retained in a similar configuration to that of bulk $FAPbI_3$.

The electronic structure of films with AALs was investigated by work function (WF) and VBM measurements using UV photoelectron spectroscopy (UPS; Fig. 3c). The WF was determined from the secondary electron cut-off, and we observed a change in WF from 4.58 to 4.41 eV after AAL modification. The VBMs were located at 1.1 and 1.3 eV below the Fermi level (E_F) for pristine films and AAL-modified films, respectively. The energy-level diagrams for the films based on the UPS and optical absorption measurement are shown in Fig. 3d. The VBM and CBM of AAL-modified films are nearly identical to those of pristine films; however, the WF shifts by about 170 meV towards the vacuum level (E_{VAC}), and the E_F shifts by 200 meV towards the CBM, indicating that the AAL-modified films become more n-type, which is likely attributable to the change of the surface termination after AAL modification[51]. Perovskite films that are more n-type have a larger number of filled electron traps, which are the predominant trap species[13,52], and this can lead to a further decrease in trap-assisted recombination events[13]. Moreover, perovskite films that are more n-type enable more efficient charge transfer between the perovskite and the electron transport material (C_{60})[51,53].

We summarized the likely mechanisms behind the device efficiency enhancement in Fig. 5. The long-chain AALs assemble on the perovskite grains, restricting the grains' tilt during growth and eventually resulting in a (100)-orientation-dominant film that is of lower defect density than a randomly oriented film (Fig. 5a,b). As the growth proceeds, the long-chain AALs are finally expelled to the perovskite film surface, as indicated by water-contact-angle measurements. The ligand layer on the perovskite film's surface provides effective surface passivation because a long-chain AAL layer enables strong hole blocking between the perovskite and C_{60} interfaces (Fig. 5c,d)[31].

Impact of AALs on device stability

Suppressing defects and performing molecular modification on perovskite grains and interfaces may have the additional effect of reducing ion migration, which is an unwanted effect in PSCs that contributes to hysteresis and low stability. We studied ion migration using temperature-dependent transient response measurements[54,55]. The ions were driven by an external bias to the electrode interface, after which this external bias was abruptly removed. A negative current can be seen due to the quick backward movement of the ion vacancies, forced by the concentration gradient (Supplementary Fig. 19). The decay rate ($1/\tau$) of the negative current reflects the ion distribution recovery time, and it was used to deduce the activation energy (E_a) of ion migration according to the following equation:

$$\ln(T/\tau) = C - \frac{E_a}{k_B T}$$

where T is the temperature, C is a constant and k_B is Boltzmann's constant.

The typical temperature-dependent transient response measurements for CsFAMA devices with AALs are shown in Supplementary Fig. 20. By fitting $\ln(T/\tau)$ versus $1/T$, we estimate an E_a of 243 meV and 422 meV for pristine films and films with AALs, respectively (Fig. 6a), indicating that ion migration is more hindered in the films with AALs.

Having shown that processing perovskite films with AALs leads to superior transport properties, and inverted PSCs with record PCEs, we sought to ascertain whether this processing strategy might compromise the operational stability of devices. To study the long-term stability of the perovskite photoactive layer, we conducted MPP tracking on encapsulated CsMAFA-8 devices under constant simulated AM1.5 illumination (100 mW cm^{-2}), as shown in Fig. 6c. Pristine devices rapidly lost 42% of their initial PCE after 350 h of testing, while the devices with AALs exhibited no PCE loss after continuous operation for 1,000 h under AM1.5 illumination. The starting device PCE was 21.2% and the final PCE after the MPP test was 21.6%. We also investigated the thermal stability by collecting J–V curves at various times for devices maintained at a fixed temperature of 85 °C. The pristine devices lost ~39% of their initial PCE while the devices with AALs lost only around 10% of their initial PCE after a thermal stability test of ~1,020 h (Fig. 6b). A reduction in defect density and ion migration likely benefited device stability[11,15].

Conclusions

In summary, we have demonstrated the role of AALs, particularly long-alkyl-chain AALs, in improving optoelectronic properties by promoting favourable grain orientations and suppressing trap-state density. Our strategy based on long-alkyl-chain AALs enabled us to demonstrate p–i–n-structured devices with >23.0% efficiency (22.3% certified) and good operational stability. The molecular modification of perovskite grains and interfaces is crucial to enhance both the efficiency and stability of PSCs. Our findings also indicated that anisotropic electronic properties of the perovskite facets make management of films' crystal orientations an important path towards high-efficiency PSCs. Further understanding of the nature of the different surface facets in polycrystalline perovskite, including the defect type and concentration, will likely be essential for the future of perovskite devices.

Methods

Materials. Unless otherwise stated, all materials were purchased from Sigma-Aldrich or Alfa Aesar and used as received. Perovskite films and devices were fabricated using PbI_2 (10-mesh beads, ultra dry, 99.999% purity) purchased from Alfa Aesar, organic halide salts purchased from GreatCell Solar and caesium iodide (99.999% purity) purchased from Sigma-Aldrich. The poly(triaryl amine) (PTAA) was purchased from Xi'an Polymer Light Technology. The C_{60} was purchase from Nano-C. The bathocuproine (BCP; sublimed grade, 99.99% purity) and all the anhydrous solvents were purchased from Sigma-Aldrich.

Perovskite film preparation and device fabrication. The patterned ITO/glass substrates were sequentially cleaned with soap, deionized water, acetone and isopropanol under ultrasonication. The ITO/glass substrates were then dried with N_2 blowing and treated with UV ozone for 15 min. The perovskite films were fabricated by the anti-solvent crystallization approach in a N_2 glove box. In a typical procedure, a hole transport layer of ~10 nm thickness made of PTAA with a concentration of 2 mg ml^{-1} dissolved in toluene was spin coated at a speed of 6,000 r.p.m for 35 s and then annealed at 100 °C for 15 min. The perovskite precursor solution (1.4 M) composed of mixed cations (Pb, Cs, FA and MA) and halides (I and Br) was dissolved in mixed solvent (DMF/DMSO = 4/1) according to a formula of $Cs_{0.05}(FA_{0.92}MA_{0.08})_{0.95}Pb(I_{0.92}Br_{0.08})_3$. A trace amount (0.1 wt%) of alkylammonium ligands (BA, PEA, OA and OAm) was added into the precursor solution. A two-step spin-coating procedure with 2,000 r.p.m. for 10 s and 4,000 r.p.m. for 50 s was adopted for the preparation of perovskite films. Chlorobenzene (150 µl) was dropped on the spinning substrate during the 45 s of the second spin-coating step. Subsequently, the sample was annealed at 100 °C for 30 min. The devices with an area of 10 mm^2 were finished by thermally evaporating C_{60} (20 nm), BCP (3 nm) and Cu (80 nm) in sequential order by using a thin-film deposition system from Angstrom Engineering under high vacuum. For the device thermal stability test, a 10-nm layer of SnO_2 and a 120-nm layer of indium zinc oxide were deposited on top of the C_{60} in sequential order, by atomic layer deposition and sputtering, respectively, to replace BCP and Cu.

Perovskite film characterizations. The SEM images were taken by a Helios G4 UX dual-beam scanning electron microscope. XRD patterns were measured with a Bruker AXS D8 diffractometer using Cu Kα radiation (λ = 1.54178 Å). The absorption spectra were obtained by a Cary 6000i UV–Vis–near-infrared spectrophotometer. The roughness was measured by an atomic force microscope (Bruker Dimension Icon with ScanAsyst). PL measurements were performed using a Horiba Fluorolog Time Correlated Single Photon Counting system with photomultiplier tube detectors. The excitation source was a pulsed laser diode at a wavelength of 504 nm. The water contact angle was measured by Drop Shape Analyzer DSA100 from KRUSS with uniform LED illumination and high-quality optics to ensure high precision when displaying the drop, to accurately measure the contact angle. GIWAXS measurements were carried out at beamline 7.3.3 of the Advanced Light Source, Lawrence Berkeley National Laboratory. Samples were measured at a detector distance of 0.249 m using an X-ray wavelength of 1.240 Å, at a 0.24° angle of incidence with respect to the substrate plane. Scattering intensity was detected by a PILATUS 2M detector.

Device characterizations. Simulated AM1.5G irradiation (100 mW cm^{-2}) was produced by a xenon-lamp-based solar simulator (Abet Technologies Sun 3000 Class AAA Solar Simulator) for J–V measurements. The light intensity was calibrated by a calibrated reference cell with a Schott visible-colour glass filter (KG5 colour filter) from Newport. A Keithley 2400 SourceMeter was used for driving the J–V measurement. The devices were measured immediately after fabrication without any preconditioning. They were measured with a metal aperture with an area of 6.69 mm^2 (certified by Newport) to accurately define the active area. A voltage scan was measured from 1.3 V to −0.3 V with a scanning rate of 0.1 V s^{-1}, and a voltage step of 10 mV was used. The devices were measured in both a nitrogen atmosphere (at KAUST) and ambient air (humidity of 30–60%; at University of Toronto) and no obvious difference was observed. To further confirm the PV parameters, the devices were measured by an independent accredited laboratory (Newport). A QSS I–V sweep protocol was used to remove the influence from the hysteresis. For the QSS I–V sweep conducted by Newport, ten voltage points were collected in the QSS measurement, and each bias voltage was applied and held until the measured current was determined to be unchanging. The J_{SC} and PCE measured by Newport were similar to the results in the lab. The EQE was measured by Newport, and the integrated J_{SC} was carefully checked and matched well with the J_{SC} from the I–V sweep before they would provide the certificate. For the transient photo-voltage measurements, the device was serially connected to a digital oscilloscope for monitoring the charge-density decay for the device

in approximately the V_{OC} condition. An attenuated 405-nm laser diode was used as a small perturbation to the background illumination on the device. The laser-pulse-induced photo-voltage variation (ΔV) and the V_{OC} were produced by the background illumination. The intensity of the short (50 ns) laser pulse was adjusted to keep the voltage perturbation below 10 mV, typically at 5 mV. A Keithley 2400 sourcemeter and a fibre integrating sphere (FOIS-1) coupled with a QE Pro spectrometer (Ocean Optics) were used for the measurements of the LED devices.

Trap density measurements by thermal admittance spectroscopy. A sinusoidal voltage ($V_{peak\text{-}to\text{-}peak}$ = 30 mV) generated from a function generator (Tektronix AFG 3000) was applied to the device. The current signal of the devices was analysed using a lock-in amplifier (Stanford Research Systems, SR830) after being amplified through a low-noise-current preamplifier (Stanford Research Systems, SR570). The capacitance of the device was calculated based on the parallel equivalent circuit model with the amplitude and phase of the current signal obtained from the lock-in amplifier. The capacitance spectra of the device were measured by scanning the frequency of the sinusoidal voltage from 0.01 to 100 kHz in logarithmic steps. The temperature of the device was controlled using a closed-cycle cryocooler (Advanced Research Systems, DE202AE). The capacitance–voltage curve was obtained by measuring the capacitance as the applied DC bias voltage was scanned from −0.2 to 1.5 V. Based on the capacitance spectra measured at different temperatures, the trap density distribution in energy (E_ω) was calculated with the following equations:

$$N_T(E_\omega) = -\frac{V_{bi}}{qW}\frac{dC}{d\omega}\frac{\omega}{k_B T} \quad (1)$$

$$E_\omega = k_B T \ln\left(\frac{\omega_0}{\omega}\right) = k_B T \ln\left(\frac{2\pi\nu_0 T^2}{\omega}\right) \quad (2)$$

where V_{bi} is the built-in potential and W is the depletion width (V_{bi} and W are derived from capacitance–voltage measurements); C is the capacitance measured at an angular frequency ω and temperature T; k_B is Boltzmann's constant and ω_0 is the attempt-to-escape frequency at temperature T; and ν_0 is a temperature-independent constant obtained by fitting the characteristic frequency at different T values with equation (2).

Ion migration measurement. To measure the ion migration activation energy, two symmetric Au electrodes were deposited on the perovskite films to form a symmetric Au/perovskite/Au device. The electrode width is 2 mm and the channel length is 50 µm. A bias voltage of 3 V was first applied to the electrodes by a source meter (Keithley 2400) for about 16 s to induce the ion migration. Then a negative current induced by the ion vacancies' redistribution could be measured after the voltage was suddenly removed. The negative current then exponentially recovered to zero. The decay time of the negative current contains the information of the ionic transport dynamics. The measurement was carried out when the temperature of the device was controlled from 280 to 325 K using a DE202AE closed-cycle cryocooler (Advanced Research Systems). Then the negative current curves were fitted with a double-exponential function. The slower decay time constants τ, which represent the ion distribution recovery time, were used to deduce the activation energy of the ion migration.

Computational methods. The DFT calculations were performed with the projector-augmented wave (PAW) method as implemented in the VASP code. The generalized gradient approximation Perdew–Burke–Ernzerhof (PBE) exchange–correlation functional was used. A uniform grid of 6×6×6 k-mesh in the Brillouin zone was employed to optimize the crystal structures of cubic-phase $FAPbI_3$. We considered $FAPbI_3$ slabs exposing different surfaces; all the slabs were separated by both top and bottom vacuum layers (~10 Å) to prevent spurious inter-slab interactions. The Brillouin zone was sampled by a 2×2×1 k-mesh for $FAPbI_3$ slabs. The plane-wave basis set cut-offs of the wavefunctions were set at 500 eV for bulk crystals and 450 eV for supercells at the generalized gradient approximation (GGA)/PBE level. The atomic positions of all supercells with and without defects were fully relaxed until the supercells had Hellman–Feynman forces on each atom of less than 0.01 eV $Å^{-1}$.

Device stability measurement. The operational stability tests were carried out at the MPP for the encapsulated devices under UV-filtered AM1.5 illumination (100 mW cm^{-2}, with a UV filter with a 420-nm cut-off). The devices were tested in a chamber with a constant nitrogen supply, which also ensured a stable device temperature of ~40 °C (the chamber itself was in ambient air). The voltage at the MPP was calculated and applied automatically; the current output of the device was tracked. The devices were encapsulated in a nitrogen glovebox. UV-curable epoxy was coated around the device area, and a glass cover slide was attached to enclose the area. The encapsulation was then finished off by exposing the construct to UV light for 10 min. The thermal stability assessment of solar cells was carried out by repeating the J–V test over various times for the devices heated at a fixed temperature of 85 °C.

Reporting Summary. Further information on research design is available in the Nature Research Reporting Summary linked to this article.

Data availability

The main data supporting the findings of this study are available within the article and its Supplementary Information. Additional data are available from the corresponding authors on reasonable request.

Received: 13 September 2019; Accepted: 13 December 2019;
Published online: 20 January 2020

References

1. Kojima, A., Teshima, K., Shirai, Y. & Miyasaka, T. Organometal halide perovskites as visible-light sensitizers for photovoltaic cells. *J. Am. Chem. Soc.* **131**, 6050–6051 (2009).
2. Yang, M. et al. Perovskite ink with wide processing window for scalable high-efficiency solar cells. *Nat. Energy* **2**, 17038 (2017).
3. Zhao, D. et al. Efficient two-terminal all-perovskite tandem solar cells enabled by high-quality low-bandgap absorber layers. *Nat. Energy* **3**, 1093–1100 (2018).
4. Wehrenfennig, C., Eperon, G. E., Johnston, M. B., Snaith, H. J. & Herz, L. M. High charge carrier mobilities and lifetimes in organolead trihalide perovskites. *Adv. Mater.* **26**, 1584–1589 (2014).
5. Shi, D. et al. Low trap-state density and long carrier diffusion in organolead trihalide perovskite single crystals. *Science* **347**, 519–522 (2015).
6. Dong, Q. et al. Electron-hole diffusion lengths > 175 µm in solution-grown $CH_3NH_3PbI_3$ single crystals. *Science* **347**, 967–970 (2015).
7. Chen, Z. et al. Single-crystal $MAPbI_3$ perovskite solar cells exceeding 21% power conversion efficiency. *ACS Energy Lett.* **4**, 1258–1259 (2019).
8. National Renewable Energy Laboratory. Best research-cell efficiencies. www.nrel.gov/pv/assets/pdfs/pv-efficiency-chart.20190103.pdf (2019).
9. Christians, J. A. et al. Tailored interfaces of unencapsulated perovskite solar cells for >1,000 hour operational stability. *Nat. Energy* **3**, 68–74 (2018).
10. Bai, S. et al. Planar perovskite solar cells with long-term stability using ionic liquid additives. *Nature* **571**, 245–250 (2019).
11. Yang, S. et al. Stabilizing halide perovskite surfaces for solar cell operation with wide-bandgap lead oxysalts. *Science* **365**, 473–478 (2019).
12. Jiang, Q. et al. Surface passivation of perovskite film for efficient solar cells. *Nat. Photonics* **13**, 460–466 (2019).
13. Luo, D. et al. Enhanced photovoltage for inverted planar heterojunction perovskite solar cells. *Science* **360**, 1442–1446 (2018).
14. Turren-Cruz, S.-H., Hagfeldt, A. & Saliba, M. Methylammonium-free, high-performance, and stable perovskite solar cells on a planar architecture. *Science* **362**, 449–453 (2018).
15. Zheng, X. et al. Defect passivation in hybrid perovskite solar cells using quaternary ammonium halide anions and cations. *Nat. Energy* **2**, 17102 (2017).
16. Bi, D. et al. Polymer-templated nucleation and crystal growth of perovskite films for solar cells with efficiency greater than 21%. *Nat. Energy* **1**, 16142 (2016).
17. Zheng, X. et al. Quantum dots supply bulk- and surface-passivation agents for efficient and stable perovskite solar cells. *Joule* **3**, 1963–1976 (2019).
18. Tong, J. et al. Carrier lifetimes of >1 µs in Sn-Pb perovskites enable efficient all-perovskite tandem solar cells. *Science* **364**, 475–479 (2019).
19. Wang, Z. et al. Efficient ambient-air-stable solar cells with 2D–3D heterostructured butylammonium-caesium-formamidinium lead halide perovskites. *Nat. Energy* **2**, 17135 (2017).
20. Deng, Y. et al. Surfactant-controlled ink drying enables high-speed deposition of perovskite films for efficient photovoltaic modules. *Nat. Energy* **3**, 560–566 (2018).
21. Li, N. et al. Cation and anion immobilization through chemical bonding enhancement with fluorides for stable halide perovskite solar cells. *Nat. Energy* **4**, 408 (2019).
22. Wang, Y. et al. Stabilizing heterostructures of soft perovskite semiconductors. *Science* **365**, 687–691 (2019).
23. Chen, M. et al. Highly stable and efficient all-inorganic lead-free perovskite solar cells with native-oxide passivation. *Nat. Commun.* **10**, 16 (2019).
24. Jao, M.-H., Lu, C.-F., Tai, P.-Y. & Su, W.-F. Precise facet engineering of perovskite single crystals by ligand-mediated strategy. *Cryst. Growth Des.* **17**, 5945–5952 (2017).
25. Muscarella, L. A. et al. Air-stable and oriented mixed lead halide perovskite (FA/MA) by the one-step deposition method using zinc iodide and an alkylammonium additive. *ACS Appl. Mater. Interfaces* **11**, 17555–17562 (2019).
26. Wu, W.-Q. et al. Bilateral alkylamine for suppressing charge recombination and improving stability in blade-coated perovskite solar cells. *Sci. Adv.* **5**, eaav8925 (2019).
27. Yang, S. et al. Tailoring passivation molecular structures for extremely small open-circuit voltage loss in perovskite solar cells. *J. Am. Chem. Soc.* **141**, 5781–5787 (2019).
28. Proppe, A. H. et al. Photochemically cross-linked quantum well ligands for 2D/3D perovskite photovoltaics with improved photovoltage and stability. *J. Am. Chem. Soc.* **141**, 14180–14189 (2019).

29. Qing, J. et al. High-quality Ruddlesden–Popper perovskite films based on in situ formed organic spacer cations. *Adv. Mater.* **31**, 1904243 (2019).
30. Fei, C. et al. Self-assembled propylammonium cations at grain boundaries and the film surface to improve the efficiency and stability of perovskite solar cells. *J. Mater. Chem. A* **7**, 23739–23746 (2019).
31. Wang, Q., Dong, Q., Li, T., Gruverman, A. & Huang, J. Thin insulating tunneling contacts for efficient and water-resistant perovskite solar cells. *Adv. Mater.* **28**, 6734–6739 (2016).
32. Lin, Y. et al. Suppressed ion migration in low-dimensional perovskites. *ACS Energy Lett.* **2**, 1571–1572 (2017).
33. Xiao, X. et al. Suppressed ion migration along the in-plane direction in layered perovskites. *ACS Energy Lett.* **3**, 684–688 (2018).
34. Yoo, J. J. et al. An interface stabilized perovskite solar cell with high stabilized efficiency and low voltage loss. *Energy Environ. Sci.* **12**, 2192–2199 (2019).
35. Zuo, L. et al. Polymer-modified halide perovskite films for efficient and stable planar heterojunction solar cells. *Sci. Adv.* **3**, e1700106 (2017).
36. Koh, T. M. et al. Enhancing moisture tolerance in efficient hybrid 3D/2D perovskite photovoltaics. *J. Mater. Chem. A* **6**, 2122–2128 (2018).
37. Yang, S. et al. Functionalization of perovskite thin films with moisture-tolerant molecules. *Nat. Energy* **1**, 15016 (2016).
38. Quintero-Bermudez, R. et al. Ligand-induced surface charge density modulation generates local type-II band alignment in reduced-dimensional perovskites. *J. Am. Chem. Soc.* **141**, 13459–13467 (2019).
39. Zhou, T. et al. Highly efficient and stable solar cells based on crystalline oriented 2D/3D hybrid perovskite. *Adv. Mater.* **31**, 1901242 (2019).
40. Liu, Y. et al. Ultrahydrophobic 3D/2D fluoroarene bilayer-based water-resistant perovskite solar cells with efficiencies exceeding 22%. *Sci. Adv.* **5**, eaaw2543 (2019).
41. Jodlowski, A. D. et al. Large guanidinium cation mixed with methylammonium in lead iodide perovskites for 19% efficient solar cells. *Nat. Energy* **2**, 972–979 (2017).
42. Jeon, N. J. et al. Solvent engineering for high-performance inorganic–organic hybrid perovskite solar cells. *Nat. Mater.* **13**, 897 (2014).
43. Yang, R. et al. Oriented quasi-2D perovskites for high performance optoelectronic devices. *Adv. Mater.* **30**, 1804771 (2018).
44. Gong, X. et al. Contactless measurements of photocarrier transport properties in perovskite single crystals. *Nat. Commun.* **10**, 1591 (2019).
45. Lee, E. M. Y. & Tisdale, W. A. Determination of exciton diffusion length by transient photoluminescence quenching and its application to quantum dot films. *J. Phys. Chem. C* **119**, 9005–9015 (2015).
46. Jariwala, S. et al. Local crystal misorientation influences non-radiative recombination in halide perovskites. *Joule* **3**, 3048–3060 (2019).
47. Zhang, L. et al. Exploring anisotropy on oriented wafers of $MAPbBr_3$ crystals grown by controlled antisolvent diffusion. *Cryst. Growth Des.* **18**, 6652–6660 (2018).
48. Kim, D. et al. Probing facet-dependent surface defects in $MAPbI_3$ perovskite single crystals. *J. Phys. Chem. C* **123**, 14144–14151 (2019).
49. Kresse, G. & Hafner, J. *Ab initio* molecular dynamics for open-shell transition metals. *Phys. Rev. B* **48**, 13115–13118 (1993).
50. Kresse, G. & Furthmüller, J. Efficient iterative schemes for *ab initio* total-energy calculations using a plane-wave basis set. *Phys. Rev. B* **54**, 11169–11186 (1996).
51. Quarti, C., De Angelis, F. & Beljonne, D. Influence of surface termination on the energy level alignment at the $CH_3NH_3PbI_3$ perovskite/C_{60} interface. *Chem. Mater.* **29**, 958–968 (2017).
52. Stranks, S. D. et al. Recombination kinetics in organic–inorganic perovskites: excitons, free charge, and subgap states. *Phys. Rev. Applied* **2**, 034007 (2014).
53. Habisreutinger, S. N., Noel, N. K., Snaith, H. J. & Nicholas, R. J. Investigating the role of 4-*tert* butylpyridine in perovskite solar cells. *Adv. Energy Mater.* **7**, 1601079 (2017).
54. Li, D. et al. Electronic and ionic transport dynamics in organolead halide perovskites. *ACS Nano* **10**, 6933–6941 (2016).
55. Pan, W. et al. $Cs_2AgBiBr_6$ single-crystal X-ray detectors with a low detection limit. *Nat. Photonics* **11**, 726–732 (2017).

Acknowledgements

We acknowledge the use of KAUST Core Lab and KAUST Solar Center facilities. This work was supported by KAUST and the Office of Sponsored Research (OSR) under award no. OSR-2017-CRG-3380. F.G. is a Wallenberg Academy Fellow.

Author contributions

O.M.B., X.Z., Y.H. and E.H.S. conceived the idea and designed the experiments. X.Z. fabricated the devices and conducted the characterizations. Y.H. contributed to device fabrication and evaluation, the MPP stability test and TRPL measurement. C.B. contributed to the measurements of thermal admittance spectroscopy, transient photo-voltage, ion migration and LEDs. J.Y. performed and interpreted the DFT calculation. J.L. performed the XRD measurements. A.K.J. performed the GIWAXS measurements. K.S., J.L., N.W., B.T. and C.Y. contributed to the electron microscopy measurements. N.G. contributed to the light-intensity-dependent *J*–*V* measurements. Y.L. contributed to the atomic force microscopy and contact angle measurements. A.Y.A. contributed to the PL measurements and PL mapping. F.Y., C.Z., Z.H., P.M., D.X., B.C. and M.W. contributed to TRPL and analyses. M.N.H. performed the UPS measurements. J.T. contributed to the stability measurements. D.B., T.D.A., Y.H., Z.H.L., O.F.M., F.G. and E.H.S. provided advice and expertise. X.Z., O.M.B., Y.H. and E.H.S. composed the manuscript. All authors discussed the results and commented on the manuscript.

Competing interests

The authors declare no competing interests.

Additional information

Supplementary information is available for this paper at https://doi.org/10.1038/s41560-019-0538-4.

Correspondence and requests for materials should be addressed to E.H.S. or O.M.B.

Reprints and permissions information is available at www.nature.com/reprints.

Publisher's note Springer Nature remains neutral with regard to jurisdictional claims in published maps and institutional affiliations.

© The Author(s), under exclusive licence to Springer Nature Limited 2020

nature research

Corresponding author(s): Edward H. Sargent and Osman M. Bakr

Solar Cells Reporting Summary

Nature Research wishes to improve the reproducibility of the work that we publish. This form is intended for publication with all accepted papers reporting the characterization of photovoltaic devices and provides structure for consistency and transparency in reporting. Some list items might not apply to an individual manuscript, but all fields must be completed for clarity.

For further information on Nature Research policies, including our data availability policy, see Authors & Referees.

Experimental design

Please check: are the following details reported in the manuscript?

1. Dimensions

Area of the tested solar cells	☒ Yes ☐ No	Methods
Method used to determine the device area	☒ Yes ☐ No	Methods

2. Current-voltage characterization

Current density-voltage (J-V) plots in both forward and backward direction	☐ Yes ☒ No	A more accurate method (quasi-steady-state (QSS) I-V sweep) was used. 10 voltage points were collected in the QSS measurement, with each bias voltage applied and held until the measured current stabilized (Supplementary Fig. 10).
Voltage scan conditions *For instance: scan direction, speed, dwell times*	☒ Yes ☐ No	Methods
Test environment *For instance: characterization temperature, in air or in glove box*	☒ Yes ☐ No	Methods
Protocol for preconditioning of the device before its characterization	☐ Yes ☒ No	Methods
Stability of the J-V characteristic *Verified with time evolution of the maximum power point or with the photocurrent at maximum power point; see ref. 7 for details.*	☒ Yes ☐ No	A more accurate method (quasi-steady-state (QSS) I-V sweep) was used. 10 voltage points were collected in the QSS measurement, with each bias voltage applied and held until the measured current stabilized (Supplementary Fig. 10).

3. Hysteresis or any other unusual behaviour

Description of the unusual behaviour observed during the characterization	☒ Yes ☐ No	Negligible hysteresis was found.
Related experimental data	☒ Yes ☐ No	Newport certification report in Supplementary Fig. 10

4. Efficiency

External quantum efficiency (EQE) or incident photons to current efficiency (IPCE)	☒ Yes ☐ No	Supplementary Fig. 10
A comparison between the integrated response under the standard reference spectrum and the response measure under the simulator	☒ Yes ☐ No	The integrated JSC from EQE spectra is consistent with the JSC from J-V measurements as certified by Newport PV Lab (Supplementary Fig. 10).
For tandem solar cells, the bias illumination and bias voltage used for each subcell	☐ Yes ☒ No	Not relevant

5. Calibration

Light source and reference cell or sensor used for the characterization	☒ Yes ☐ No	Methods
Confirmation that the reference cell was calibrated and certified	☒ Yes ☐ No	Methods

Calculation of spectral mismatch between the reference cell and the devices under test	☒ Yes ☐ No	It has been calibrated.

6. Mask/aperture

Size of the mask/aperture used during testing	☒ Yes ☐ No	Methods
Variation of the measured short-circuit current density with the mask/aperture area	☐ Yes ☒ No	Newport certification report in Supplementary Fig. 9 and Supplementary Fig. 10

7. Performance certification

Identity of the independent certification laboratory that confirmed the photovoltaic performance	☒ Yes ☐ No	Certified by Newport PV Lab
A copy of any certificate(s) *Provide in Supplementary Information*	☒ Yes ☐ No	Newport certification report in Supplementary Fig. 9

8. Statistics

Number of solar cells tested	☒ Yes ☐ No	At least 100 devices were tested (Fig. 2).
Statistical analysis of the device performance	☒ Yes ☐ No	Figure 2

9. Long-term stability analysis

Type of analysis, bias conditions and environmental conditions *For instance: illumination type, temperature, atmosphere humidity, encapsulation method, preconditioning temperature*	☒ Yes ☐ No	Figure 6